Fast and high resolution mapping of elastic properties of biomolecules and polymers with bimodal AFM

Simone Benaglia, Victor G. Gisbert, Alma P. Perrino, Carlos A. Amo and Ricardo Garcia

Materials Science Factory

Instituto de Ciencia de Materiales de Madrid (ICMM), CSIC

c/ Sor Juana Ines de la Cruz 3

28049 Madrid, Spain

email address: r.garcia@csic.es

Fast, high resolution and wide elastic modulus range mapping of heterogeneous interfaces represents a major goal of atomic force microscopy (AFM). This goal becomes more challenging when the nanomechanical mapping involves biomolecules in their native environment. Over the years, several AFM-based methods have been developed to address that goal. However, none of those methods combine sub-nanometer spatial resolution, quantitative accuracy, fast data acquisition speed, wide elastic modulus range and operation in physiological solutions. Here we present detailed protocols to generate high resolution maps of the elastic properties of biomolecules and polymers by using bimodal AFM. The method is fast because the elastic modulus, deformation and topography images are obtained simultaneously. The method is efficient because just a single data point per pixel is needed to generate the above images. In addition, by knowing the deformation, bimodal AFM enables to reconstruct the true topography of the surface.

INTRODUCTION

Fast, non-invasive, high resolution and label free characterization methods are needed to understand the whole range of biomolecular interactions and/or to develop hybrid materials with tailored properties at the nanoscale. The atomic force microscope (AFM)[1] has significantly contributed to our current understanding of biomolecular interactions and soft-matter interfaces[2-5]. In fact, to generate high resolution nanomechanical maps of heterogeneous surfaces represents one of the major goals of force microscopy. Two factors make the nanoscale characterization of biomolecules in physiological solutions very challenging. Biomolecules are soft materials. The force exerted by the probe on a biomolecule causes the vertical and lateral deformation, that in turn, worsens the spatial resolution. On the other hand, hydrodynamic effects and the presence of a variety of electrolytes and/or solvent molecules in the liquid disturb the interactions between the probe and the sample.

Ideally, a method to provide nanomechanical maps of biomolecules and polymers should have the following features. (1) Quantitative accuracy. (2) Sub-nanometer spatial resolution. (3) Characterization independent of the probe properties. (4) Compatible with high speed data acquisition. (5) Absence of cross-talk between topography and material properties.

The development of multifrequency AFM has provided new approaches to map material properties at the nanoscale[6-15]. Here we describe how a bimodal atomic force microscope enables the simultaneous mapping of the Young's modulus, the deformation and the true topography of biomolecules and polymers in their native environment[16]. The Young's modulus is determined with a relative error below 5% over a five order of magnitude range (1 MPa-100 GPa). Numerical simulations and calibration tests validate the accuracy of the method. This method requires a single data point per pixel to generate simultaneously the true topography and the elastic map of a biomolecule in liquid. The above feature speeds up data acquisition while minimizing the amount of data used in the measurements.

The procedure explains how a bimodal AFM generates true topographic and elastic modulus maps of biomolecules and polymers over a modulus range from 1 MPa to 100 GPa. In the first stage (Steps 1-5), we describe the preparation of samples, a block copolymer, a membrane protein and a single protein that illustrate the performance of bimodal AFM. In the second stage (Steps 6-10), we describe the procedure to calibrate the spring constants of the microcantilever. In the third stage (Steps 11-17), the microscope parameters are selected and the imaging process is accomplished. Finally, we present the elastic, deformation and true topography maps of the three samples (Steps 18-21).

Current methods to map mechanical properties at the nanoscale

Force microscopy has generated a variety of methods to measure mechanical properties with high spatial resolution. Those approaches could be broadly classified in two categories: force-distance curve and parametric methods. Force-distance curve methods are based on the measurement of the dependence of the force with respect to the tip-sample distance on each point of the surface[17-18]. From a force-distance curve the Young's modulus is obtained by fitting the repulsive section of the force-distance curve with a model of the interaction force (contact mechanics). The acquisition and representation of arrays of force-distance curves, one per pixel of the surface, is usually known as force volume images[17]. Torsional harmonics[10-11] or peak force tapping could be also included in this category.

Force-distance curves are obtained in quasi-static or dynamic excitation of the cantilever. In the quasi-static case, the tip-surface distance is modulated at a frequency much smaller than the fundamental cantilever resonance. Force-distance curves obtained in the quasi-static regime are widely used to measure the elastic modulus of soft and hard interfaces at the nanoscale[17-21]. In fact, it is the most common nanomechanical characterization method. However, this approach has several drawbacks. Force-distance curve AFM imaging is intrinsically slow. The modulation frequency cannot be increased arbitrarily because of the inertial and hydrodynamic effects associated with the cantilever dynamics[22]. The sensitivity of a force-distance curve depends on the cantilever spring constant. The cantilever must be selected according to the expected elastic response of the material. It would be hard to apply this approach to map the local elasticity of heterogeneous surfaces made of regions with significantly different elastic properties. In addition, the acquisition of a force-distance curve requires to collect a large number of data points per pixel to retrieve the material properties with reasonable accuracy.

Force-distance curves could also be obtained when the cantilever is excited near a resonant frequency[23-26]. Of the resonance methods, the approach based on analysing the time-resolved response of the cantilever has attracted more attention[10-11,23]. This approach requires the measurements of the higher harmonics components of the cantilever deflection. The generation of higher harmonics usually demands the application of forces in the tens or hundreds of nN. Those forces could either damage the sample or blunt the tip. The use of T-shaped cantilevers[10] enables the detection of higher harmonics components at lower forces. Torsional harmonics has been applied to measure the mechanical properties of some synthetic and biological membranes at sub-nN forces[27-28]. However, T-shaped cantilevers are hard to manufacture and calibrate.

Parametric nanomechanical methods are associated with the excitation and/or detection of the cantilever at a resonant frequency or higher frequencies. In a parametric method, the observables of the microscope are directly connected (parameterized) to certain mechanical properties. These approaches require the use of a theoretical framework. Bimodal[29-31] and contact resonance methods[32-34] provide examples of parametric nanomechanical measurements.

In bimodal AFM, the observables associated with the excited modes are very sensitive to changes in the tip-sample distance. The observables of the 1st and the 2nd modes explore different spatial ranges of the interaction force[35-36]. From a mathematical perspective, bimodal AFM enables to describe the dynamics of the AFM by matching the number of unknowns and equations. Those features have opened a variety of applications that range from the atomic resolution imaging of surfaces in liquid[37-39] and ultra high vacuum[40-41], to imaging of buried nanostructures[42-44], to separate mechanical and electromagnetic interactions[45-47], to mapping the surface force vector field[41] or to transduce an optical signal into a mechanical force[48-49]. More specifically, bimodal AFM has increased the nanoscale characterization capabilities of the AFM to detect compositional variations on soft matter such as polymers[50-51], proteins[52-55], lipid layers[56], DNA[57-58], virus[59] or cells[60-61]. The method has also stimulated the design of very sensitive cantilevers[62-66] and a rich theoretical activity[67-73].

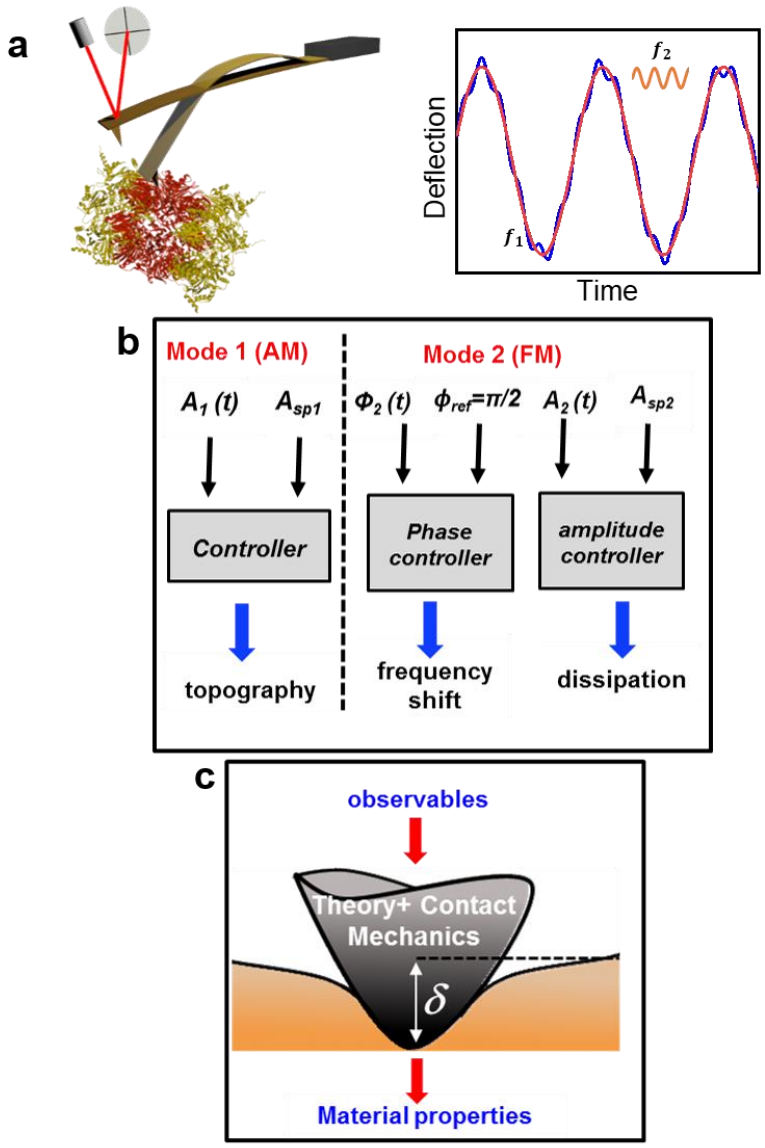

Figure 1. Bimodal AM-FM. (a) Scheme of the cantilever deflection in bimodal AFM. The deflection signal has two components. The low frequency component is tuned at the 1st resonant frequency of the cantilever while the high frequency component is tuned at the 2nd resonant frequency. (b) Simplified scheme of the feedback loops in bimodal AM-FM. The topography feedback operates on the amplitude of the 1st mode. The phase shift of the 2nd mode is kept at 90º with respect to the driving force while A_2 is kept at a fixed value (A_{sp2}). The last step is achieved by varying the driving force of the 2nd mode. (c) Simplified scheme of the transformation of bimodal data into nanomechanical properties.

Overview of bimodal AFM

Bimodal AFM uses two driving forces to oscillate the cantilever (**Fig. 1a**). The excitation frequencies of the driving forces are tuned to match two of the eigenmodes of the cantilever, usually the 1st and the 2nd flexural modes. In the presence of a sample, the tip response is decomposed in terms of the components oscillating at the frequencies of the two excited modes. The variety of observables (amplitude, phase shift and resonant frequency shift), feedbacks loops acting on the modes (amplitude or frequency) and the type of cantilever modes involved (flexural or torsional) has produced several bimodal AFM configurations[74-77]. This variety makes bimodal AFM very flexible and, at the same time, complex. Numerical simulations[6] laid the foundations for the experimental implementation of bimodal AFM. Simulations and theory[16,31,35,36,67,69,78] are applied to define its accuracy to measure nanomechanical properties. A guide to the different bimodal AFM configurations is given in ref. 77.

In bimodal AFM, the driving force applied to the microcantilever is

$$F_d = F_1 \cos(2\pi f_1 t) + F_2 \cos(2\pi f_2 t) \quad (1)$$

where F_n and f_n are, respectively, the driving force and frequency of the *n*-th mode.

In the bimodal configuration described in this protocol, the amplitude of the 1st mode is used as a feedback signal for controlling the tip-sample distance (AM). This feedback control generates an apparent image of the topography of the sample. A second feedback acts on the signal of the 2nd mode by tracking the shift in its resonant frequency (FM). At the same time, the driving force of the 2nd mode is controlled to keep the oscillation amplitude of the 2nd mode at a fixed value. This bimodal configuration combines the robustness and simplicity of AM operation with the sensitivity and signal-to-noise ratio of FM operation. To our best knowledge, this is the more robust and sensitive of the current bimodal AFM configurations for quantitative mapping. In addition, the use of an AM feedback to track the topography makes it compatible with high-speed imaging[79]. This bimodal configuration is technically called bimodal AM-FM, however, for the purpose of this protocol, we will call it bimodal AFM.

From observables to material properties

In bimodal AM-FM, the oscillation of the 1st mode is controlled with an amplitude modulation feedback while the oscillation of the 2nd mode is controlled with a frequency modulation feedback (**Figure 1b**). The transformation of experimental observables into elastic properties is divided in two major steps. First, the theory that provides the relationship among the experimental observables and the maximum tip-surface force (peak force). The second step involves expressing the peak force in terms of the indentation and the effective Young's modulus by using a contact mechanics model (**Figure 1c**).

The tip deflection in bimodal AM-FM can be approximated by

$$z(t) = z_0 + \sum_n A_n \cos(\omega_n t - \phi_n) \approx z_0 + A_1 \cos(\omega_1 t - \phi_1) + A_2 \cos(\omega_2 t - \frac{\pi}{2}) \quad (2)$$

where z_0, A_n, $\omega_n=2\pi f_n$ and ϕ_n are, respectively, the mean deflection, the amplitude, the angular frequency and the phase shift of the *n*-th mode. The tip-surface force includes a repulsive force as described by Sneddon contact mechanics[80]

$$F_{Sneddon} = \alpha E_{eff} \delta^{\beta} \quad (3)$$

E_{eff} is expressed in terms of sample Young's modulus and Poisson coefficient ν_s by

$$E_{eff} \approx \frac{E_s}{(1-\nu_s^2)} \quad (4)$$

In Eq. 4 we have considered that the tip's Young's modulus is much larger than the one of the polymers and biomolecules. δ is the sample deformation; α is a coefficient that depends on the tip's geometry and size and β is a coefficient that depends on the tip's geometry. For a paraboloid tip in contact with a half space elastic material, the values of the above coefficients are $\alpha=4/3R^{1/2}$ and $\beta=3/2$.

For common axisymmetric AFM probes (paraboloid, cone and cylinder), the effective Young's modulus and the sample deformation are related to the bimodal AFM observables by the following expressions. For a paraboloid (radius *R*)

$$E_{eff} = \frac{4\sqrt{2}}{\sqrt{R}} Q_1 \, k_1 \left(\frac{k_2 \Delta f_2}{k_1 f_{02}}\right)^2 \frac{{A_1}^{3/2}}{A_{01}^2 - A_1^2} \quad (5)$$

$$\delta = \frac{1}{2}\delta_N \quad (6)$$

For a cone (half angle θ),

$$E_{eff} = \frac{3\pi^2\sqrt{10}}{50 \tan\theta} \, {Q_1}^{\frac{3}{2}} k_1 \left(\frac{k_2 \Delta f_2}{k_1 f_{02}}\right)^{5/2} \frac{{A_1}^2}{\left(A_{01}^2 - A_1^2\right)^{3/2}} \quad (7)$$

$$\delta = \frac{5}{4}\delta_N \quad (8)$$

For a cylinder of radius *R*

$$E_{eff} = \frac{2\pi\sqrt{3}}{3R} \sqrt{Q_1} \, k_1 \left(\frac{k_2 \Delta f_2}{k_1 f_{02}}\right)^{3/2} \frac{A_1}{\left(A_{01}^2 - A_1^2\right)^{1/2}} \quad (9)$$

$$\delta = \frac{3}{8}\delta_N \quad (10)$$

To determine the deformation, we have used the following

$$\delta_N = \frac{1}{Q_1}\frac{k_1}{k_2}\frac{f_{02}}{\Delta f_2}(A_{01}^2 - A_1^2)^{1/2} \qquad (11)$$

where k_i and Q_i are the spring constant and quality factor of the mode i; A_{01} and A_1 are, respectively, the free amplitude and the set-point amplitude of the 1st mode; f_{02} and Δf_2 are the free resonant frequency and frequency shift of 2nd mode. We remark that a single observable $\Delta f_2(x,y)$ carries the information about the local changes of the Young's modulus and the deformation. The other parameters that appear in the above equations (k_1, k_2, Q_1, A_{01}, A_1, R and f_{02}) are set at the beginning of the experiment. The accuracy of the nanomechanical measurements is highly dependent on the calibration of the above parameters (**Fig. 2**, Steps 6-10).

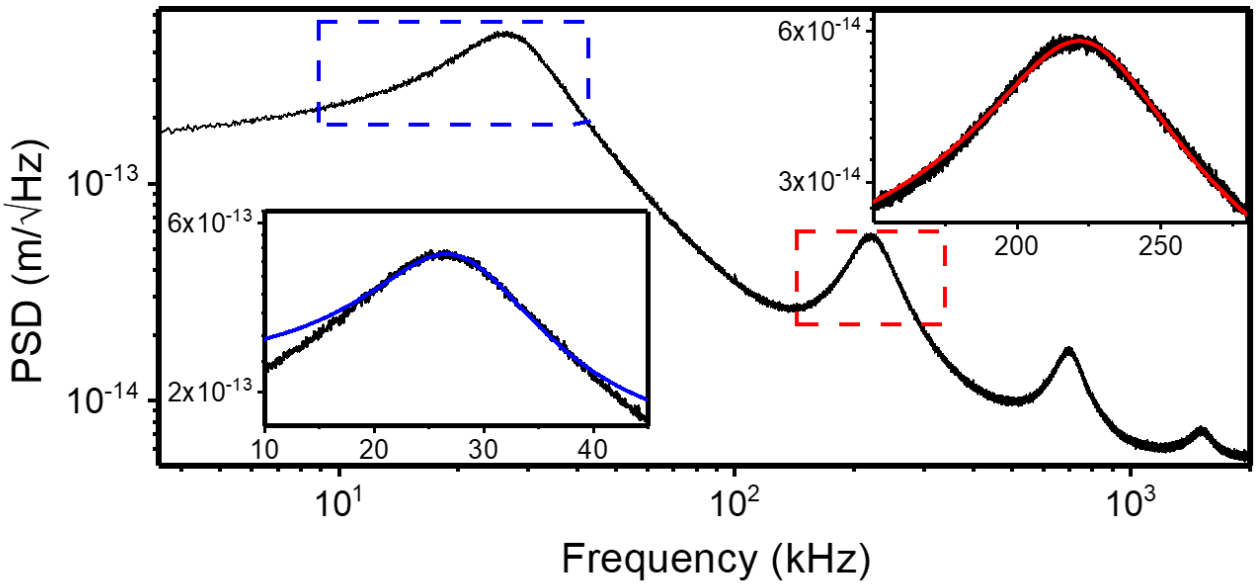

Figure 2. Calibration of the spring constants and quality factors by using the thermal noise spectra. Power spectral density of a microcantilever (BL-AC40TS) excited by the thermal noise in liquid. The first four resonances are observed. The insets show the fitting of the PSD of the first two modes to the expression of a single harmonic oscillator.

True and apparent topography

Currently, the AFM signal that is converted into a topography image assumes that the sample has not been deformed during the imaging process. This is a valid approximation for imaging rigid materials (say those with a Young's modulus above 10 GPa) under the application of peak forces below 5 nN. On soft matter interfaces, the force applied by the tip produces significant deformations. Those deformations needed to obtain the true topography of the surface. In general, the raw image generated from the AFM feedback controls can only be considered as an apparent topographic image.

The effect of the force on the deformation of the sample has been reported on polymers[81-82] and biomolecules[83-84]. However, to our best knowledge, very few attempts have been implemented to reconstruct the true topography of a soft matter sample from the AFM data[30,82]. In standard AFM configurations (single mode excitation and detection), it is very hard to separate the apparent topography and the deformation signals. Bimodal AFM solves this issue in a straightforward manner by introducing an additional equation to relate the observables to the deformation. A true topography image is generated once the local deformation of the surface is known.

Spatial, material property and time resolutions

Bimodal AFM operation does not introduce any restriction on the spatial and/or temporal resolutions of force microscopy. Several examples have illustrated the advantages of bimodal AFM to enhance the material contrast on heterogeneous surfaces[9]. Atomic resolution images have been reported for different types of materials and environments (liquid, air and vacuum)[37-38,40-41].

The accuracy of bimodal AFM on the determination of the elastic modulus on a given material will depend on the suitability of the Sneddon contact mechanics to describe the deformation of the material. Numerical simulations[16] show that for Sneddon contact mechanics materials, the relative error of bimodal AM-FM to determine the elastic modulus is below 5%.

MATERIALS

REAGENTS

- Analytical-grade buffers (4-(2-hydroxyethyl)-1-piperazineethanesulfonic acid, HEPES, Sigma-Aldrich; tris(hydroxymethyl)aminomethane, Tris; Sigma-Aldrich)
- Analytical-grade electrolytes ($MgCl_2$, Sigma-Aldrich; KCl, Sigma-Aldrich; HCl, Sigma-Aldrich)
- Ethanol, Sigma-Aldrich
- PGMEA, Sigma-Aldrich
- Human 20S proteasome, Enzo Life Sciences
- Native Purple membrane from *Halobacterium salivarum*
- *Poly(styrene-block-methyl methacrylate)*, PS-b-PMMA (M_{PS}= 18.1 kg mol^{-1} and M_{PMMA}= 24.2 kg mol^{-1}, PDI= 1.1)
- *Poly(styrene-random-methyl methacrylate)*, PS-r-PMMA (M_R= 7.9 kg mol^{-1}, PDI= 1.1, with a styrene fraction of 58%)
- Si wafer
- Acetone, Sigma-Aldrich

EQUIPMENT

- Mica (natural Muscovite mica, Alpha Biotech)
- Mica punch set, Precision Brand
- Steel disc
- Teflon foil
- Teflon-compatible chemically inert two-component epoxy glue (Araldite)
- Air-gun with filter and tubing to connect to the nitrogen outlet
- Oxygen Plasma
- Spin Coater
- Oven
- pH meter, HANNA Instruments
- Oscilloscope, Tektronix
- Mechanical vibration analyzer (HWL Scientific Instruments) **▲ CRITICAL** Vibrational and acoustic isolation is crucial in high resolution experiments.
- Type of cantilever depends on the chosen sample (for polymers, e.g. PPP-FM or PPP-NCHAuD, Nanosensors, for biological samples, RC800PSA or BL-AC40TS, Olympus). **▲ CRITICAL** The choice of the cantilever will influence the final result, in terms of topographical and nanomechanical resolution.
- Cypher microscope (Oxford Instrument, Asylum Research). Asylum Research offers an already developed Atomic Force Microscopy system for bimodal AM-FM. **▲ CRITICAL** Temperature control systems have to be preferred in order to avoid thermal drift during the measurement.

REAGENT SETUP

Buffer solutions: ▲ CRITICAL It is important to make and stock all the solutions in clean materials otherwise they could result contaminated.

Adsorption buffer for Purple Membrane is 10 mM Tris-HCl, 150 mM KCl, 25 mM $MgCl_2$ (pH 7.2). It can be stored at 4 °C for a few months.
Imaging buffer for Purple Membrane is 10 mM Tris- HCl, 150 mM KCl (pH 7.2). It can be stored at 4 °C for a few months.

Adsorption buffer for 20S proteasome is 50mM Hepes-KOH, 100mM KCl, 5mM $MgCl_2$ (pH 7.5). It can be stored at 4 °C for a few months.
Imaging buffer for 20S proteasome is 25mM Hepes-KOH, 100mM KCl (pH 7.5). It can be stored at 4 °C for a few months.

EQUIPMENT SETUP

Atomic force microscope with dual excitation scheme The AFM system has to provide the possibility to excite and detect the cantilever in two of its eigenmodes (usually the 1st and 2nd). The hardware provided by Asylum Research already includes the dual excitation system. The software included in the setup can be used to analyze the data obtained in the measurements.

PROCEDURE

Preparation of Block copolymer samples ● TIMING ~ 3 h

1| Dissolve the PS-r-PMMA and PS-b-PMMA in PGMEA to a 1.5 wt%.

2| Spin Coat (5000 rpm for 30 s) the PS-r-PMMA on the Si wafer surface, previously treated by Oxygen plasma and leave it annealing for 10 min at ~200°C. Rinse the sample with PGMEA to remove the first polymer layers.

3| Spin coat the PS-b-PMMA solution (2500 rpm for 30 s) and let the annealing for 10 min at ~200°C.

▲ CRITICAL STEP The procedure has to be done in a clean room to ensure the quality of the final result. This procedure could be used to prepare different possible geometries (lamellar, cylindrical, etc.) depending on the characteristics of the random and block copolymers. In this paper we show block copolymer thin films with a lamellar geometry[85-86] and a 23.4 nm pitch (**Fig. 4a**).

Preparation of Mica disks ● TIMING ~ 25 min

4| Punch the mica sheet using the puncher set to produce mica disks with a diameter of 3.2 mm for single proteins measurements and 15 mm for the membrane proteins. **▲ CRITICAL STEP** The use of a small mica disks for imaging single proteins is crucial to ensure the even distribution of the proteins over the surface. The mica is glued with epoxy to the Teflon foil.

Buffer Preparation and adsorption of proteins ● TIMING ~ 2-3 h

5| Prepare all the solutions using Milli-Q water, analytical grade buffers and electrolytes. Cleave the mica disc using Scotch tape in order to obtain a uniform layer. **▲ CRITICAL STEP** To avoid contaminations in the sample, cleave the mica just before adding the buffer and proteins.

a) 2D membrane proteins (Purple Membrane) preparation

i) Dilute the purple membrane with the deposition buffer to reach a concentration of 40 μg ml^{-1}. Then, deposit 15 μl of solution on a circular piece of freshly cleaved mica for 15 min. Finally, rinse it gently with the imaging buffer.

b) Single Protein (20S proteasome) preparation

i) Add adsorption buffer in order to obtain ~100 nM concentration of proteins. Deposit 8 μl of the solution covering the mica sheet. The proteasome sample must rest for 20 minutes for adsorption of the mica surface. Rinse gently with the measurement buffer. **▲ CRITICAL STEP** Due to the weak binding between the

mica and the proteins, the concentration on top of the mica must be adjusted to reach a stable coverage of proteins.

? TROUBLESHOOTING

Select the proper AFM cantilever ● TIMING ~ 10-15 min

6| The imaging of the block copolymer was performed with a relatively stiff cantilever like the PPP-FM ($k_1 \sim 5$ N m^{-1}), or PPP-NCH ($k_1 \sim 40$ N m^{-1}). For softer samples like those of purple membrane or single proteins, we have chosen softer cantielver with a sharp tip's radius (BL-AC40TS). The spring contants of this cantilever ($k_1 \sim 0.08$ N m^{-1}) facilitates the imaging of biological samples at low forces (below 500 pN). **▲ CRITICAL STEP** Choosing the right cantilever facilitates the achievement of high resolution topography and elastic modulus images.

Setup of the Microscope ● TIMING ~ 30-40 min

7| **▲ CRITICAL STEP** If you are using an Asylum Research microscope, follow this instruction from Step 7. If not go to Step 8. Put the sample on the microscope stage and the tip in position to start the measurement. Select the bimodal AM-FM interface in the software. Before starting the measurement, take a thermal spectrum of the cantilever in order to measure the resonant frequencies of the 1st and 2nd modes.

? TROUBLESHOOTING

8| Depending on the environment (liquid or air) use the proper method for driving the oscillation of the cantilever[87-88] (**Fig. 3**):

a) In air: use the acoustic excitation (piezo drive) to excite the cantilever.

b) In water: fill the space between the sample and the tip holder with the measurement buffer. If available, use photothermal excitation to avoid unwanted mechanical resonances from the fluid cell. Optimize the position of the excitation laser spot at the back end of the cantilever (**Fig. 3a**). The laser spot position is the same for the two modes.

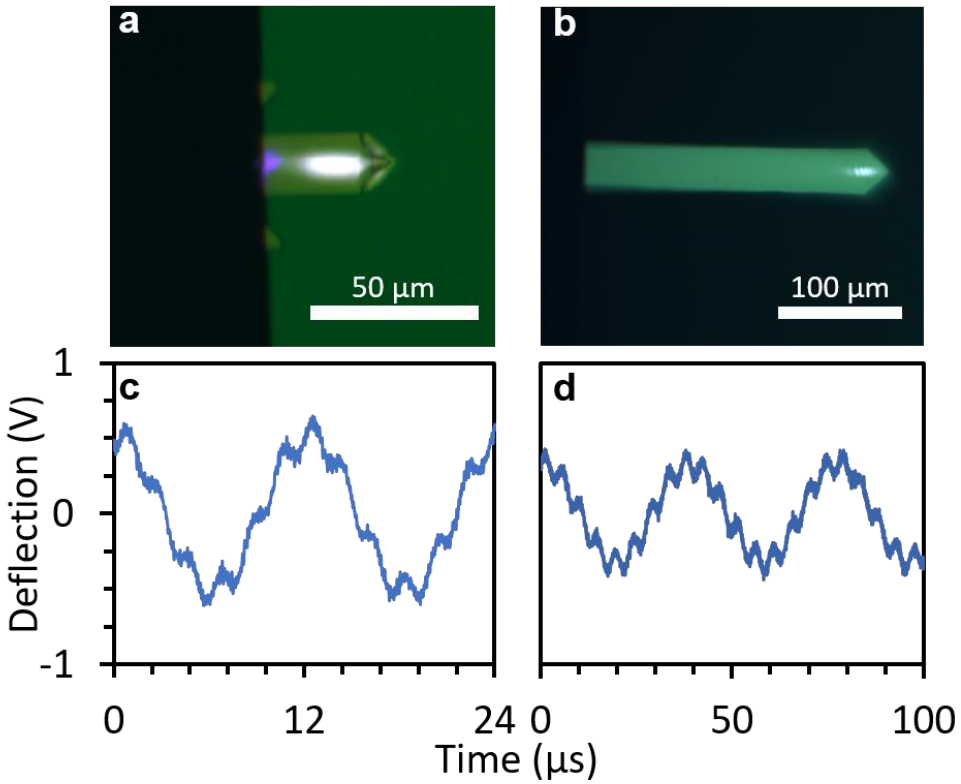

Figure 3. Cantilever excitation in bimodal AM-FM. (**a**) Optical microscope images of BL-AC40TS and (**b**) PPP-FM cantilevers. The BL-AC40TS is driven by photothermal excitation (purple spot in **a**) in a buffer solution. The PPP-FM is excited acoustically (piezo actuator) in air. (**c**, **d**) Measured deflection voltage (photodiode) of the cantilevers operated in bimodal AM-FM. The signal is recorded by an oscilloscope.

Cantilever calibration ● TIMING **~ 10-15 min**

9| The calibration of the spring constant and optical sensitivity of the 1st and 2nd mode is necessary in order to obtain maps of the elastic interaction. The optical lever sensitivity (nm V^{-1}) of the 1st mode is obtained by acquiring a deflection-distance curve on a stiff surface (Muscovite mica). Once optical lever sensitivity is known, the PSD (**Fig. 2**) of the thermal motion of the cantilever is fitted to the simple harmonic oscillator (SHO)

$$|A_{thermal}(\omega)|^2 = A_{white}^2 + \frac{A^2\omega_0^4}{\left(\omega^2-\omega_0^2\right)^2+\omega^2\omega_0^2/Q^2} \quad (12)$$

Where A is the amplitude, ω_0 is the angular resonant frequency, ω the angular driving frequency, Q the quality factor and A_{white} the white noise. Then, the spring constant $k_1 = 2k_BT/(\pi A f_0 Q)$.

▲ **CRITICAL STEP** To avoid damaging the tip, we recommend to perform the calibration of the spring constant at the end of the experiment, i.e. Step 17, as a requirement for high resolution images.

10| The spring constant of the 2nd mode, k_2, was calibrated by assuming the stiffness-frequency power law relationship given by[89]

$$k_2 = k_1 \left(\frac{f_2}{f_1}\right)^{\zeta_2} \quad (13)$$

where ζ_2 is an experimental calibration parameter, determined by the geometry of the cantilever.

▲ **CRITICAL STEP** In ref. 89, the calibration of the 2nd mode is obtained with the parameter ζ_2 calibrated for a specific model of cantilever. For the PPP-NCH the value is $\zeta_2 = 2.13$ while for the PPP-FM is $\zeta_2 = 2.13$. The value used for the BL-AC40TS is $\zeta_2 = 2.0$. The latter coefficient is the default theoretical value used for rectangular cantilevers.

? TROUBLESHOOTING

AFM measurement in tapping mode ● TIMING ~ 15-30 min

11| Far from the sample, tune the 1st and the 2nd mode and set the phase shifts to 90° for both modes.

12| Set the free and setpoint amplitudes of the 1st mode and initialize the tip approach. Once the tip engaged to the surface, check the value of the phase shift: a requirement for the nanomechanical mapping is to keep the phase of the 1st mode always below 90°, resulting in a repulsive contact between the tip and the sample.

!CAUTION Avoid tip damage during the approach.

13| Record a 5 x 5 μm image to check the state of the sample. Use a small scanning frequency in the fast axis (1-2 Hz) to avoid crashing the tip. For biological samples, choose an area covered by proteins and zoom for the bimodal measurement.

!CAUTION Keep the amplitude setpoint as close as possible to the free amplitude value to reduce the force applied. Sample and/or tip deformation could be significant by using setpoint value far from the free amplitude.

High resolution bimodal mapping ● TIMING more than 2 hours

14| For polymers, the measurements were done in air with a free amplitude of ~90 nm. To ensure that the imaging is performed in the repulsive regime, use a setpoint of below than 75% of the free amplitude. **▲ CRITICAL STEP** If you don't achieve a stable repulsive regime, increase the free amplitude until you do not observe any more attractive interaction.

15| For biological samples in aqueous solution, start the measurement with A_{01} ~5 nm and $A_1 \approx 0.9 \cdot A_{01}$ to ensure low forces[29]. The details of the topography should be resolved with high resolution. Modify the values of A_{01} and A_1 until a good image of the proteins is obtained. Typical parameters of measurement are a scan size of 400 nm, a scan rate of ~5 Hz (fast axis) and a number of points per line of 512. **▲ CRITICAL STEP** Adjusting the feedback gains of the 1st mode is crucial in order to achieve high resolution. Low values are recommended.

16| The determination of the Young's modulus map requires to record the local changes of the frequency shift of the 2nd mode. Set A_2 ~0.5 nm and adjust the FM feedback. The gain parameters of the frequency feedback, which keeps ϕ_2=90º by changing the driving frequency, should be increased until the frequency channel resolves some relevant features of the sample, without the presence of oscillations or random noise. Then, an auxiliary feedback keeps A_2 constant by adjusting the driving force on the 2nd mode. This auxiliary feedback is called dissipation in the AFM community. During the recording of the topography and frequency shift, A_1 must be readjusted to obtain high resolution maps (**Fig. 4**).

▲ CRITICAL STEP The parameters used in amplitude modulation to achieve high resolution topographical images must be adjusted when activating the 2nd mode for the bimodal AM-FM measurement as A_2 will affect the peak force and thus the quality of the image.

!CAUTION Increasing the amplitude of the 2nd mode will improve the quality of the elastic modulus map. However, A_2 should be less than 10% of A_1[9,31].

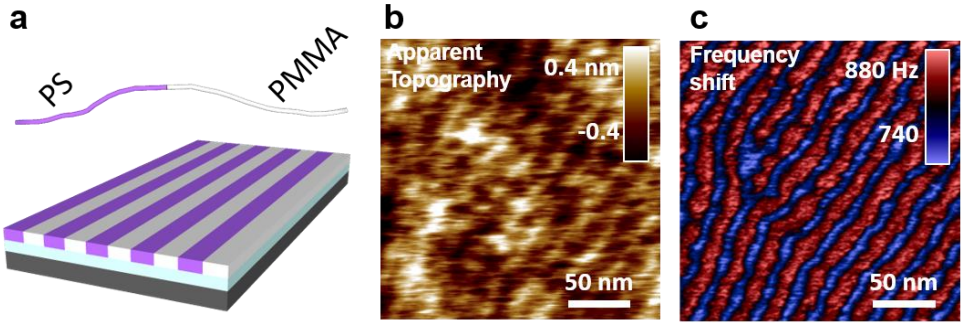

Figure 4. Bimodal AFM images of a block copolymer. (**a**) Scheme of the lamellar PS-b-PMMA block copolymer. (**b**) Apparent topography (feedback on the amplitude of the 1st mode). (**c**) 2nd mode frequency shift map. PPP-FM cantilever characterized by f_1 = 82 kHz, k_1 = 3 N m^{-1}, Q_1 = 220, f_2 = 518 kHz and k_2 = 152 N m^{-1}, R = 2 nm; Other parameters A_{01} = 95 nm, A_1 = 70 nm and A_2 = 1 nm. Images obtained in air.

17| If the image does not show any improvement by increasing the zoom or the number of points, the resolution limit is reached. This limit is defined by the sample conditions, tip and imaging parameters (scan rate, amplitude and gains of the 1st and the 2nd mode). **▲ CRITICAL STEP** The tip's geometry and chemical properties greatly influence the spatial resolution. The tip radius should be smaller than the features of the sample to be imaged. Changes of the tip require to repeat the experiments until high resolution data are achieved. Bimodal AFM demands an optimization of the parameters in order to get high resolution and contrast images from both modes at the same time.

? TROUBLESHOOTING

Nanomechanical reconstruction and data analysis ● TIMING ~ 20 min

18| The bimodal AM-FM data must be processed in order to obtain the Young's modulus and the deformation maps of the sample. The processing also enables to determine the peak force applied during the measurement. Here, the experimental data have been processed by assuming a paraboloid tip. The Young's modulus and the deformation have been calculated by using, respectively, Equations 5 and 6. In all cases we have assumed a Poisson coefficient ν_s=0.3.

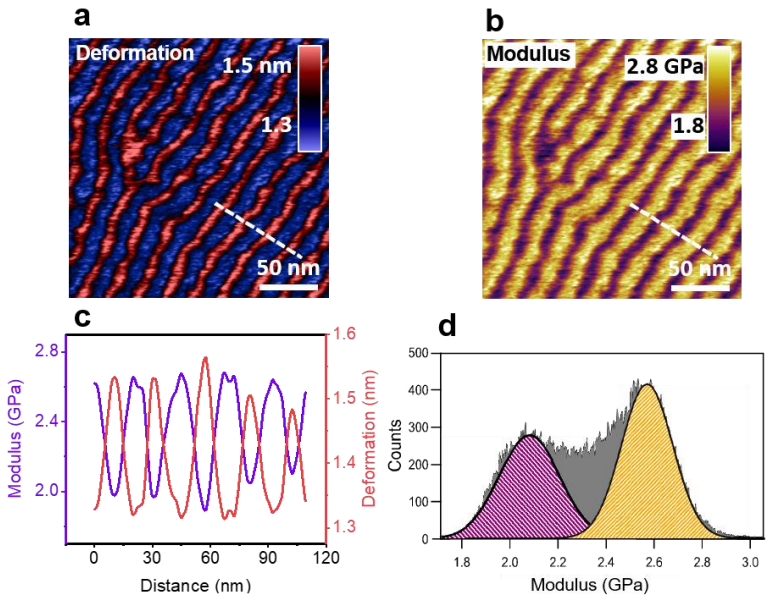

Figure 5. Elastic modulus and deformation maps. (**a**) Deformation map in a block copolymer (PS-b-PMMA) thin film. (**b**) Map of the Young's modulus of PS-b-PMMA**. (c)** Cross-section along the dashed lines. **(d)** Histogram of the Young's modulus obtained from **b**. Maps were obtained by applying a peak force of 8.5 nN (PS) and 8.9 nN (PMMA).

19| According to Equations (5,6,11) changes in Δf_2 (**Fig. 4c**) can only be related to a difference in the Young's modulus of the sample. **▲ CRITICAL STEP** To calculate the Young's modulus the offset values f_{02} and A_{01} have to be measured during the imaging. Those values are determined by measuring the dependencies of A_1 and f_2 versus *z*-piezo displacement. From the frequency *z*-piezo displacement curve we obtain the minimum frequency f_2 (minimum). This value is considered the free resonant frequency f_{02}. Then, the frequency shift is calculated as $\Delta f_2 = f_2 - f_{02}$. The *z*-piezo displacement corresponding to f_2(minimum) is used to find the value A_1, that is considered as A_{01}.

20| The true topography of the surface is obtained (**Fig. 6b**) by adding the deformation and apparent topography images.

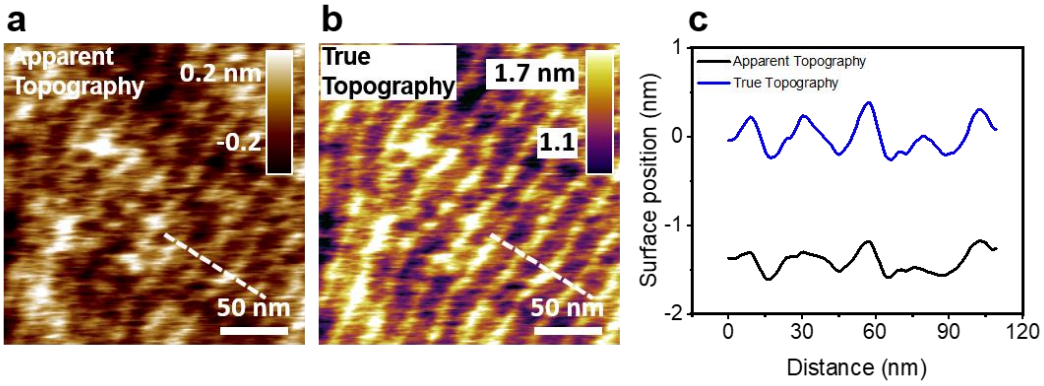

Figure 6. Apparent to and true topographic maps. (**a**) Apparent topography. (**b**) True topography reconstructed from the apparent topography and the deformation maps. (**c**) Cross sections across the dashed lines. In the apparent topography image, the surface is about 1.5 nm below is unperturbed baseline.

21| The high resolution data obtained are processed in the following way:

a) Purple membrane images (**Fig. 7**) are corrected with a cross-correlation averaging. First, one bacteriorhodopsin (BR) trimer is selected and cross-correlated with the topography image. From the cross-correlation each individual BR trimer is located. Second, the coordinates of each BR trimer are merged with the elastic modulus, deformation and dissipation channels. Finally, each unit cell is superimposed, averaged and three-fold symmetrized to obtain the corresponding insets.

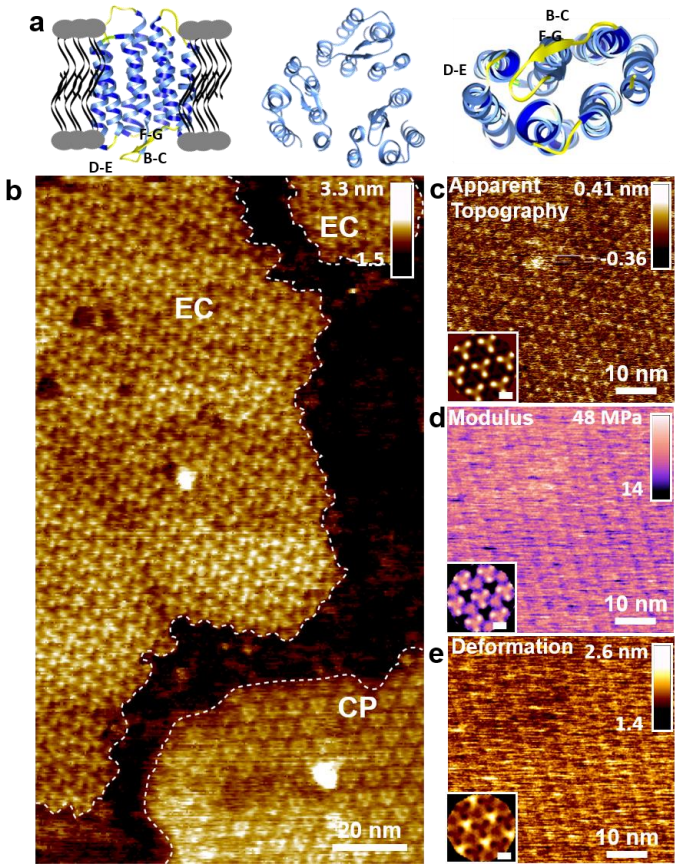

Figure 7. Bimodal AFM maps of a purple membrane in buffer. (**a**) Scheme of the protein BR organization within the purple membrane. (**b**) Topography of several PM patches showing the extracellular and the cytoplasmic sides of the membrane. (**c**) High resolution image of an EC region of the membrane. The hexagonal arrangement of the BR trimers is resolved. (**d**) Young's modulus map of the region shown in **b**. The image (raw data) shows the existence of parallel stripes with a spacing of 6.2 nm. (**e**) Deformation map of the region shown in **b**. Bimodal AFM images obtained by applying a peak force of 200 pN. Data adapted from ref. 16.

b) For the 20S proteasome picture, the image of a single protein is selected. The symmetrical structure of the protein is used to perform the cross correlation. An average is done by adding the original image, the original image flipped with respect to the vertical axis, the original image flipped with respect to horizontal axis and, the original image flipped with respect to the vertical and horizontal axes. Then, trace and the retrace are averaged, and a Gaussian filter is applied. The resulting images of the topography and Young's Modulus of the proteasome are shown in **Figures 8**.

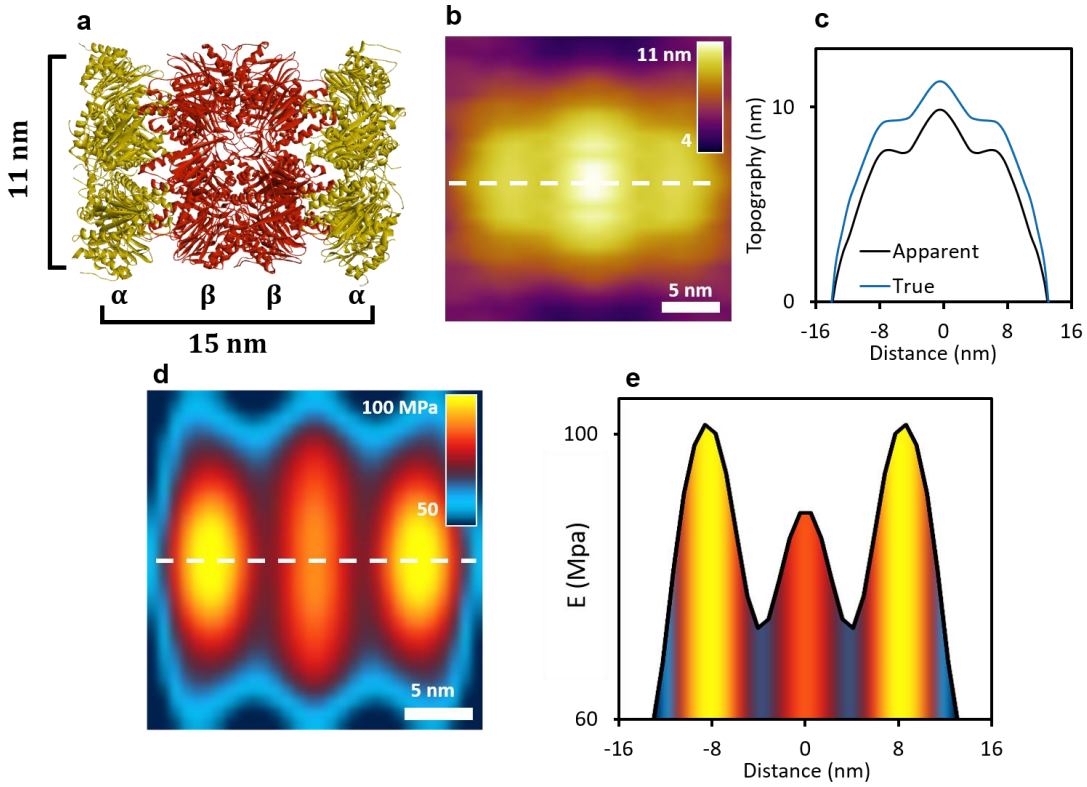

Figure 8. Bimodal AFM maps of a 20S proteasome in liquid. (**a**) Scheme of the 20S proteasome (Protein Data Bank 5L4G). (**b**) True topography, reconstructed from the apparent topography and deformation maps. (**c**) Cross-sections along the marked lines in the true and the apparent (not shown) topography images. (**d**) Young's modulus map. (**e**) The structural section (α subunits) gives a value 100 MPa while the catalytic region (β subunits) gives an average value of 89 MPa. Bimodal AFM images were obtained by applying a peak force of 430 pN. The BL-AC40TS is characterized by $f_1 = 29$ kHz, $k_1 = 0.084$ N m^{-1}, $Q_1 = 1.9$, $f_2 = 243$ kHz and $k_2 = 3.3$ N m^{-1}, $R = 2$ nm; the measurement conditions were $A_{01} = 5.0$ nm, $A_1 = 3.8$ nm and $A_2 = 0.5$ nm.

? Troubleshooting

Buffer Preparation and adsorption of proteins (Step 5)

To get high resolution bimodal AFM images the protein absorption should be optimized[90]. The formation of protein multilayers or aggregates should be avoided. At low coverages, the proteins could be displaced laterally by the tip.

Set up of the microscope (Step 7)

Position of the laser The thermal noise spectrum depends on the position of the laser along the main axis of the cantilever[91]. If the amplitude (PSD) of one of the normal modes is small, it can be increased by optimizing the laser spot position on the cantilever (especially for the 2nd mode).

Cantilever calibration (Step 11)

Sampling time of thermal noise The calibration is a crucial step to determine the nanomechanical properties; long sampling times are recommended to acquire good PSD spectra.

High resolution bimodal mapping (Step 14 to 17)

The topography is unstable and there is bad tip-sample contact Increase the scan size to obtain a more stable image and then go back to the initial scan size.

The proteins layer is not stable over the measurement Increase the value of the setpoint amplitude to reduce the applied force. If the force is too high the protein could be damage or displaced laterally. It is also recommended to increase the scan rate to reduce the contact time.

Tip contamination High resolution images require the very sharp and stable (mechanical and chemical) tips and the optimization of the imaging parameters. Sometimes the tip's performance improves during the imaging process. If the resolution of the image is good but some small features are not resolved, it is advice to keep imaging with the same tip. When a tip fails to resolve the main features of the biomolecule (~10 nm) it is advised to change it or expose it to UV light for ~30 min.

Optimization of topography and Young's modulus channel During bimodal AM-FM imaging the quality of the topography measurement could be affected by the parameters of the 2nd mode. The signal to noise-ratio obtained in the 2nd mode image should be optimized to get high resolution contrast. This optimization step might affect the quality of the height image in the 1st mode. A balance between the contrast in both modes must be reached.

Anticipated Results

These protocols show how bimodal AM-FM generates high resolution images of the elastic modulus and the true topography of soft matter surfaces. The elastic modulus, deformation and topography images are obtained simultaneously. The method allows to measure the elastic response of a wide modulus range of materials from soft biomolecules in their native environments to rigid surfaces. Here bimodal AFM has been applied to measure polymeric and biological samples, such as PS-b-PMMA block copolymer, purple membrane and 20S proteasome. Those samples are representative of many soft matter interfaces. The measurements are performed by exciting the cantilever with two signals tuned to 1st and the 2nd mode frequencies. Two feedback loops control the imaging process. One keeps the amplitude of the 1st mode at a fixed value (AM) while the other keeps the phase shift of the 2nd mode at a

constant value (FM). Those loops provide an apparent image of the topography and a frequency shift map. Those signals are transformed into Young's modulus, deformation and true topography images by using a theoretical framework (Equation 5,6,11).

From these results, we show that the structural and catalytic units of the 20S proteasome have different Young's modulus. We also report local changes of the Young's modulus across the protein loops joining the α-helix domains in the protein forming the purple membrane structure. The wide application range of the method is illustrated by identifying the regions of a block copolymer according to the Young's modulus values. The spatial resolution of the elastic modulus maps on soft matter samples (1 MPa to 5 GPa) is of 1 nm.

Acknowledgment

We thank the financial support from the European Research Council ERC–AdG– 340177 (3DNanoMech) and the Ministerio de Economía y Competitividad for grants CSD2010-00024 and MAT2016-76507-R. This work has received funding from the European Union's Horizon 2020 research and innovation programme under the Marie Sklodowska-Curie grant agreement No.721874 (SPM2.0). The fellowships FPU15/04622 and BES-2017-081907 from the Ministerio de Educación are also acknowledged.

Author contributions

S.B., V.G.G and A.P.P. performed the experiments. C.A.A. deduced the analytical expressions. S.B. and V.G.G. drafted the procedure. R.G. designed the experiments, supervised the theory, wrote the introduction and edited the manuscript. All the authors discussed the results and revised the Ms.

Data and code availability

The data and computer code that support the findings of this study are available from the corresponding author upon reasonable request.

Competing interests

The authors declare no competing interests.

References

1. Binnig, G., Quate, C. F. & Gerber, C. Atomic Force Microscope. *Phys. Rev. Lett.* **56**, 930–933 (1986).

2. Dufrêne, Y. F. et al. Imaging modes of atomic force microscopy for application in molecular and cell biology. *Nat. Nanotechnol.* **12**, 295–307 (2017).

3. Garcia, R., Magerle, R. & Perez, R. Nanoscale compositional mapping with gentle forces. *Nat. Mater.* **6**, 405–411 (2007).

4. Proksch, R. et al. Practical loss tangent imaging with amplitude-modulated atomic force microscopy. *J. Appl. Phys.* **119**, 134901 (2016).

5. Wang, D. & Russell, T. P. Advances in Atomic Force Microscopy for Probing Polymer Structure and Properties. *Macromolecules* **51**, 3–24 (2018).

6. Rodriguez, T. R. & Garcia, R. Compositional mapping of surfaces in atomic force microscopy by excitation of the second normal mode of the microcantilever. *Appl. Phys. Lett.* **84**, 449–451 (2004).

7. Martinez, N. F., Patil, S., Lozano, J. R. & Garcia, R. Enhanced compositional sensitivity in atomic force microscopy by the excitation of the first two flexural modes. *Appl. Phys. Lett.* **89**, 2–4 (2006).

8. Proksch, R. Multifrequency, repulsive-mode amplitude-modulated atomic force microscopy. *Appl. Phys. Lett.* **89**, 1–4 (2006).

9. Garcia, R. & Herruzo, E. T. The emergence of multifrequency force microscopy. *Nat. Nanotechnol.* **7**, 217–226 (2012).

10. Raman, A. et al. Mapping nanomechanical properties of live cells using multi-harmonic atomic force microscopy. *Nat. Nanotechnol.* **6**, 809–814 (2011).

11. Sahin, O., Magonov, S., Su, C., Quate, C. F. & Solgaard, O. An atomic force microscope tip designed to measure time-varying nanomechanical forces. *Nat. Nanotechnol.* **2**, 507–514 (2007).

12. Zhang, S., Aslan, H., Besenbacher, F. & Dong, M. Quantitative biomolecular imaging by dynamic nanomechanical mapping. *Chem. Soc. Rev.* **43**, 7412–7429 (2014).

13. Santos, S., Lai, C.-Y., Olukan, T. & Chiesa, M. Multifrequency AFM: from origins to convergence. *Nanoscale* **9**, 5038–5043 (2017).

14. Platz, D., Tholén, E. A., Pesen, D. & Haviland, D. B. Intermodulation atomic force microscopy. *Appl. Phys. Lett.* **92**, 153106 (2008).

15. Jesse, S., Kalinin, S. V., Proksch, R., Baddorf, A. P. & Rodriguez, B. J. The band excitation method in scanning probe microscopy for rapid mapping of energy dissipation on the nanoscale. *Nanotechnology* **18**, 435503 (2007).

16. Amo, C. A., Perrino, A. P., Payam, A. F. & Garcia, R. Mapping Elastic Properties of Heterogeneous Materials in Liquid with Angstrom-Scale Resolution. *ACS Nano* **11**, 8650–8659 (2017).

17. Heinz, W. F. & Hoh, J. H. Spatially resolved force spectroscopy of biological surfaces using the atomic force microscope. *Trends Biotechnol.* **17**, 143–150 (1999).

18. Dufrêne, Y. F., Martínez-Martín, D., Medalsy, I., Alsteens, D. & Müller, D. J. Multiparametric imaging of biological systems by force-distance curve–based AFM. *Nat. Methods* **10**, 847–854 (2013).

19. Young, T. J. et al. The use of the PeakForceTMquantitative nanomechanical mapping AFM-based method for high-resolution Young's modulus measurement of polymers. *Meas. Sci. Technol.* **22**, 125703 (2011).

20. Dokukin, M. E. & Sokolov, I. Quantitative mapping of the elastic modulus of soft materials with HarmoniX and PeakForce QNM AFM modes. *Langmuir* **28**, 16060–16071 (2012).

21. Pfreundschuh, M., Martinez-Martin, D., Mulvihill, E., Wegmann, S. & Muller, D. J. Multiparametric high-resolution imaging of native proteins by force-distance curve-based *AFM. Nat. Protoc*. **9**, 1113–1130 (2014).

22. Amo, C. A. & Garcia, R. Fundamental High-Speed Limits in Single-Molecule, Single-Cell, and Nanoscale Force Spectroscopies. *ACS Nano* **10**, 7117–7124 (2016).

23. Stark, M., Stark, R. W., Heckl, W. M. & Guckenberger, R. Inverting dynamic force microscopy: From signals to time-resolved interaction forces. *Proc. Natl. Acad. Sci.* **99**, 8473–8478 (2002).

24. Shamitko-Klingensmith, N., Molchanoff, K. M., Burke, K. A., Magnone, G. J. & Legleiter, J. Mapping the mechanical properties of cholesterol-containing supported lipid bilayers with nanoscale spatial resolution. *Langmuir* **28**, 13411–13422 (2012).

25. Platz, D., Forchheimer, D., Tholén, E. A. & Haviland, D. B. Interaction imaging with amplitude-dependence force spectroscopy. *Nat. Commun.* **4**, 1360 (2013).

26. Payam, A. F., Martin-Jimenez, D. & Garcia, R. Force reconstruction from tapping mode force microscopy experiments. *Nanotechnology* **26**, 1–12 (2015).

27. Dong, M., Husale, S. & Sahin, O. Determination of protein structural flexibility by microsecond force spectroscopy. *Nat. Nanotechnol.* **4**, 514–517 (2009).

28. Lü, J., Yang, J., Dong, M. & Sahin, O. Nanomechanical spectroscopy of synthetic and biological membranes. *Nanoscale* **6**, 7604–7608 (2014).

29. Martinez-Martin, D., Herruzo, E. T., Dietz, C., Gomez-Herrero, J. & Garcia, R. Noninvasive protein structural flexibility mapping by bimodal dynamic force microscopy. *Phys. Rev. Lett.* **106**, 1–4 (2011).

30. Herruzo, E. T., Perrino, A. P. & Garcia, R. Fast nanomechanical spectroscopy of soft matter. *Nat. Commun.* **5**, 3126 (2014).

31. Labuda, A., Kocun, M., Meinhold, W., Walters, D. & Proksch, R. Generalized Hertz model for bimodal nanomechanical mapping. *Beilstein J. Nanotechnol.* **7**, 970–982 (2016).

32. Rabe, U. et al. Imaging and measurement of local mechanical material properties by atomic force acoustic microscopy. *Surf. Interface Anal.* **33**, 65–70 (2002).

33. Killgore, J. P. et al. Viscoelastic property mapping with contact resonance force microscopy. *Langmuir* **27**, 13983–13987 (2011).

34. Tetard, L., Passian, A. & Thundat, T. New modes for subsurface atomic force microscopy through nanomechanical coupling. *Nat. Nanotechnol.* **5**, 105–109 (2010).

35. Kawai, S. et al. Systematic achievement of improved atomic-Scale contrast via bimodal dynamic force microscopy. *Phys. Rev. Lett.* **103**, 1–4 (2009).

36. Herruzo, E. T. & Garcia, R. Theoretical study of the frequency shift in bimodal FM-AFM by fractional calculus. *Beilstein J. Nanotechnol.* **3**, 198–206 (2012).

37. Herruzo, E. T., Asakawa, H., Fukuma, T. & Garcia, R. Three-dimensional quantitative force maps in liquid with 10 piconewton, angstrom and sub-minute resolutions. *Nanoscale* **5**, 2678–2685 (2013).

38. Ebeling, D. & Solares, S. D. Amplitude modulation dynamic force microscopy imaging in liquids with atomic resolution: comparison of phase contrasts in single and dual mode operation. *Nanotechnology* **24**, 135702 (2013).

39. Ooe, H. et al. Amplitude dependence of image quality in atomically-resolved bimodal atomic force microscopy. *Appl. Phys. Lett.* **109**, 141603 (2016).

40. Kawai, S., Eren, B., Marot, L. & Meyer, E. Graphene synthesis via thermal polymerization of aromatic quinone molecules. *ACS Nano* **8**, 5932–5938 (2014).

41. Naitoh, Y. et al. Subatomic-scale force vector mapping above a Ge(001) dimer using bimodal atomic force microscopy. *Nat. Phys.* **13**, 663–667 (2017).

42. Ebeling, D., Eslami, B. & Solares, S. D. J. Visualizing the subsurface of soft matter: Simultaneous topographical imaging, depth modulation, and compositional mapping with triple frequency atomic force microscopy. *ACS Nano* **7**, 10387–10396 (2013).

43. Thompson, H. T., Barroso-Bujans, F., Herrero, J. G., Reifenberger, R. & Raman, A. Subsurface imaging of carbon nanotube networks in polymers with DC-biased multifrequency dynamic atomic force microscopy. *Nanotechnology* **24**, 135701 (2013).

44. Perrino, A. P., Ryu, Y. K., Amo, C. A., Morales, M. P. & Garcia, R. Subsurface imaging of silicon nanowire circuits and iron oxide nanoparticles with sub-10 nm spatial resolution. *Nanotechnology* **27,** 275703 (2016).

45. Li, J. W., Cleveland, J. P. & Proksch, R. Bimodal magnetic force microscopy: Separation of short and long range forces. *Appl. Phys. Lett.* **94**, 163118 (2009).

46. Dietz, C., Herruzo, E. T., Lozano, J. R. & Garcia, R. Nanomechanical coupling enables detection and imaging of 5 nm superparamagnetic particles in liquid. *Nanotechnology* **22**, 125708 (2011).

47. Schwenk, J. et al. Bimodal magnetic force microscopy with capacitive tip-sample distance control. *Appl. Phys. Lett.* **107**, 132407 (2015).

48. Nowak, D. et al. Nanoscale chemical imaging by photoinduced force microscopy. *Sci. Adv.* **2**, e1501571–e1501571 (2016).

49. Ambrosio, A., Devlin, R. C., Capasso, F. & Wilson, W. L. Observation of Nanoscale Refractive Index Contrast via Photoinduced Force Microscopy. *ACS Photonics* **4**, 846–851 (2017).

50. Nguyen, H. K., Ito, M. & Nakajima, K. Elastic and viscoelastic characterization of inhomogeneous polymers by bimodal atomic force microscopy. *Jpn. J. Appl. Phys*. **55**, 08NB06 (2016).

51. Dietz, C. Sensing in-plane nanomechanical surface and sub-surface properties of polymers: local shear stress as function of the indentation depth. *Nanoscale* **10**, 460–468 (2018).

52. Bubendorf, A., Walheim, S., Schimmel, T. & Meyer, E. A robust AFM-based method for locally measuring the elasticity of samples. *Beilstein J. Nanotechnol.* **9**, 1–10 (2018).

53. Patil, S., Martinez, N. F., Lozano, J. R. & Garcia, R. Force microscopy imaging of individual protein molecules with sub-pico Newton force sensitivity. *J. Mol. Recognit.* **20**, 516–523 (2007).

54. Lamour, G., Yip, C. K., Li, H. & Gsponer, J. High Intrinsic Mechanical Flexibility of Mouse Prion Nanofibrils Revealed by Measurements of Axial and Radial Young's Moduli. *ACS Nano* **8**, 3851–3861 (2014).

55. Ricci, M., Quinlan, R. A. & Voïtchovsky, K. Sub-nanometre mapping of the aquaporin–water interface using multifrequency atomic force microscopy. *Soft Matter* **13**, 187–195 (2017).

56. Al-Rekabi, Z. & Contera, S. Multifrequency AFM reveals lipid membrane mechanical properties and the effect of cholesterol in modulating viscoelasticity. *Proc. Natl. Acad. Sci.* **115**, 2658–2663 (2018).

57. Lai, C. Y., Santos, S. & Chiesa, M. Systematic Multidimensional Quantification of Nanoscale Systems from Bimodal Atomic Force Microscopy Data. *ACS Nano* **10**, 6265–6272 (2016).

58. Bose, K., Lech, C. J., Heddi, B. & Phan, A. T. High-resolution AFM structure of DNA G-wires in aqueous solution. *Nat. Commun.* **9**, 1959 (2018).

59. González-Domínguez, I., Gutiérrez-Granados, S., Cervera, L., Gòdia, F. & Domingo, N. Identification of HIV-1–Based Virus-like Particles by Multifrequency Atomic Force Microscopy. *Biophys. J.* **111**, 1173–1179 (2016).

60. Cartagena-Rivera, A. X., Wang, W. H., Geahlen, R. L. & Raman, A. Fast, multi-frequency, and quantitative nanomechanical mapping of live cells using the atomic force microscope. *Sci. Rep.* **5**, 1–11 (2015).

61. Guan, D., Charlaix, E., Qi, R. Z. & Tong, P. Noncontact Viscoelastic Imaging of Living Cells Using a Long-Needle Atomic Force Microscope with Dual-Frequency Modulation. *Phys. Rev. Appl.* **8**, 1–10 (2017).

62. Martinez, N. F. et al. Bimodal atomic force microscopy imaging of isolated antibodies in air and liquids. *Nanotechnology* **19**, 384011 (2008).

63. Loganathan, M. & Bristow, D. A. Bi-harmonic cantilever design for improved measurement sensitivity in tapping-mode atomic force microscopy. *Rev. Sci. Instrum.* **85**, 043703 (2014).

64. Dietz, C., Schulze, M., Voss, A., Riesch, C. & Stark, R. W. Bimodal frequency-modulated atomic force microscopy with small cantilevers. *Nanoscale* **7**, 1849–1856 (2015).

65. Penedo, M. et al. Selective enhancement of individual cantilever high resonance modes. *Nanotechnology* **26**, 485706 (2015).

66. Ruppert, M. G. & Moheimani, S. O. R. High-bandwidth multimode self-sensing in bimodal atomic force microscopy. *Beilstein J. Nanotechnol.* **7**, 284–295 (2016).

67. Lozano, J. R. & Garcia, R. Theory of multifrequency atomic force microscopy. *Phys. Rev. Lett.* **100**, 8–11 (2008).

68. Stark, R. W. Bistability, higher harmonics, and chaos in AFM. *Mater. Today* **13**, 24–32 (2010).

69. Aksoy, M. D. & Atalar, A. Force spectroscopy using bimodal frequency modulation atomic force microscopy. *Phys. Rev. B* **83**, 075416 (2011).

70. Lozano, J. R., Kiracofe, D., Melcher, J., Garcia, R. & Raman, A. Calibration of higher eigenmode spring constants of atomic force microscope cantilevers. *Nanotechnology* **21**, 465502 (2010).

71. Forchheimer, D., Platz, D., Tholén, E. A. & Haviland, D. B. Model-based extraction of material properties in multifrequency atomic force microscopy. *Phys. Rev. B* **85**, 1–7 (2012).

72. An, S., Solares, S. D., Santos, S. & Ebeling, D. Energy transfer between eigenmodes in multimodal atomic force microscopy. *Nanotechnology* **25,** 475701 (2014).

73. Santos, S. Phase contrast and operation regimes in multifrequency atomic force microscopy. *Appl. Phys. Lett.* **104**, 143109 (2014).

74. Solares, S. D. & Chawla, G. Triple-frequency intermittent contact atomic force microscopy characterization: Simultaneous topographical, phase, and frequency shift contrast in ambient air. *J. Appl. Phys.* **108**, 054901 (2010).

75. Chawla, G. & Solares, S. D. Mapping of conservative and dissipative interactions in bimodal atomic force microscopy using open-loop and phase-locked-loop control of the higher eigenmode. *Appl. Phys. Lett.* **99**, 074103 (2011).

76. Naitoh, Y., Ma, Z., Li, Y. J., Kageshima, M. & Sugawara, Y. Simultaneous observation of surface topography and elasticity at atomic scale by multifrequency frequency modulation atomic force microscopy. J. Vac. Sci. Technol. B, Nanotechnol. Microelectron. *Mater. Process. Meas. Phenom.* **28**, 1210–1214 (2010).

77. Garcia, R. & Proksch, R. Nanomechanical mapping of soft matter by bimodal force microscopy. *Eur. Polym. J.* **49**, 1897–1906 (2013).

78. Lozano, J.R. & Garcia, R. Theory of phase spectroscopy in bimodal atomic force microscopy. *Phys. Rev. B* **79**, 014110 (2009)

79. Uchihashi, T., Kodera, N. & Ando, T. Guide to video recording of structure dynamics and dynamic processes of proteins by high-speed atomic force microscopy. *Nat. Protoc.* **7**, 1193–1206 (2012).

80. Sneddon, I. N. The relation between load and penetration in the axisymmetric Boussinesq problem for a punch of arbitrary profile. *Int. J. Eng. Sci.* **3**, 47–57 (1965).

81. Knoll, R., Magerle, K. & Krausch, G. Tapping Mode atomic force microscopy on polymers: Where is the true sample surface? *Macromolecules* **34**, 4159–4165 (2001).

82. Wang, D., Fujinami, S., Nakajima, K. & Nishi, T. True surface topography and nanomechanical mapping measurements on block copolymers with atomic force microscopy. *Macromolecules* **43,** 3169–3172 (2010).

83. San Paulo, A. & Garcia, R. High-Resolution Imaging of Antibodies by Tapping-Mode Atomic Force Microscopy: Attractive and Repulsive Tip-Sample Interaction Regimes. *Biophys. J.* **78**, 1599–1605 (2000).

84. Perrino, A. P. & Garcia, R. How soft is a single protein? The stress–strain curve of antibody pentamers with 5 pN and 50 pm resolutions. *Nanoscale* **8**, 9151–9158 (2016).

85. Gottlieb, S. et al. Thermal scanning probe lithography for the directed self-assembly of block copolymers. *Nanotechnology* **28**, 175301 (2017).

86. Gottlieb, S. et al. Nano-confinement of block copolymers in high accuracy topographical guiding patterns: modelling the emergence of defectivity due to incommensurability. Soft Matter, (2018)

87. Umeda, N., Ishizaki, S. & Uwai, H. Scanning attractive force microscope using photothermal vibration. *J. Vac. Sci. Technol. B* **9**, 1318 (1991).

88. Herruzo, E. T. & Garcia, R. Frequency response of an atomic force microscope in liquids and air: Magnetic versus acoustic excitation. *Appl. Phys. Lett.* **91,** 89–92 (2007).

89. Labuda, A. et al. Calibration of higher eigenmodes of cantilevers. *Rev. Sci. Instrum.* **87**, 073705 (2016).

90. Rabe, M., Verdes, D. & Seeger, S. Understanding protein adsorption phenomena at solid surfaces. *Adv. Colloid Interface Sci.* **162**, 87–106 (2011).

91. Butt, H.-J. & Jaschke, M. Calculation of thermal noise in atomic force microscopy. *Nanotechnology* **6**, 1–7 (1995).